

Graphene and boron nitride lateral heterostructures for atomically thin circuitry

Mark P. Levendorf^{1*}, Cheol-Joo Kim^{1*}, Lola Brown¹, Pinshane Y. Huang², Robin W. Havener², David A. Muller^{2,3} & Jiwoong Park^{1,3}

Precise spatial control over the electrical properties of thin films is the key capability enabling the production of modern integrated circuitry. Although recent advances in chemical vapour deposition methods have enabled the large-scale production of both intrinsic and doped graphene^{1–6}, as well as hexagonal boron nitride (*h*-BN)^{7–10}, controlled fabrication of lateral heterostructures in these truly atomically thin systems has not been achieved. Graphene/*h*-BN interfaces are of particular interest, because it is known that areas of different atomic compositions may coexist within continuous atomically thin films^{5,10} and that, with proper control, the bandgap and magnetic properties can be precisely engineered^{11–13}. However, previously reported approaches for controlling these interfaces have fundamental limitations and cannot be easily integrated with conventional lithography^{14–16}. Here we report a versatile and scalable process, which we call ‘patterned regrowth’, that allows for the spatially controlled synthesis of lateral junctions between electrically conductive graphene and insulating *h*-BN, as well as between intrinsic and substitutionally doped graphene. We demonstrate that the resulting films form mechanically continuous sheets across these heterojunctions. Conductance measurements confirm laterally insulating behaviour for *h*-BN regions, while the electrical behaviour of both doped and undoped graphene sheets maintain excellent properties, with low sheet resistances and high carrier mobilities. Our results represent an important step towards developing atomically thin integrated circuitry and enable the fabrication of electrically isolated active and passive elements embedded in continuous, one-atom-thick sheets, which could be manipulated and stacked to form complex devices at the ultimate thickness limit.

Figure 1a summarizes our approach for the patterned regrowth and characterization. After growing the first film of graphene (*G*¹, superscript representing the growth order), we then deposit a protective layer of photoresist and pattern away unwanted areas. Next we grow a second layer of graphene or *h*-BN (*G*²/*h*-BN²) and transfer the hybrid film onto the desired substrate for further characterization. All of our growths are performed on Cu foil using standard literature recipes for both graphene and *h*-BN growths^{4,5,8}. Introducing dopant gases during any graphene growth stage allows us to produce both intrinsic graphene (*i*-G; H₂ + CH₄) and *n*-doped graphene (*n*-G; NH₃ + H₂ + CH₄) in a single process run (see Supplementary Information). Figure 1b shows optical images of the Cu growth substrate at different steps of the process. After patterning the first graphene layer, the substrate was heated to 135 °C in air to enhance the contrast, as is shown in Fig. 1b (left panel); the areas of Cu protected by *i*-G¹ remain unoxidized whereas the unprotected areas do not¹⁷. Figure 1b (right panel) shows the same foil after reduction of CuO_x and subsequent synthesis of the second graphene, and demonstrates the homogeneity of the Cu/graphene substrate. Before further characterization, the presence of graphene is confirmed using micro-Raman spectroscopy (see Supplementary Information).

The fidelity of the transferred pattern and the quality of the junctions formed by our method were studied using dark-field transmission

electron microscopy (DF-TEM)^{18,19}, where use of a specific objective aperture filter allows imaging of areas with corresponding lattice orientations. Multiple such images can then be coloured and overlaid to form a complete map of the film, resolving the grain structure and number of layers with nanometre-scale resolution, both near to and away from the junction area. Figure 1c shows a composite image of a graphene sample that includes both the first and second grown areas as well as the junction between the two. For this, growths of *i*-G¹/*i*-G² were transferred onto 10-nm-thick Si₃N₄ TEM membranes. Both *G*¹ and *G*² regions (see inset to Fig. 1c) comprise single crystals of similar sizes, which indicates that the polycrystalline structure of the graphene is determined mainly by the synthesis conditions rather than the growth order, and also that the structure of the first grown graphene is unaffected by our patterned regrowth. Significantly, the location of the junction closely follows the designed pattern within the resolution of our instrument (partially outlined area in Fig. 1c; see Supplementary Information).

Our DF-TEM data and electrical characterization, in addition to the growth conditions, suggest that the junction between *G*¹ and *G*² areas are laterally connected. Our recent work²⁰ has shown that a more-reactive growth environment produces graphene–graphene grain boundaries with high-quality lateral connections and minimal inter-domain electrical resistance, whereas a less-reactive growth environment results in poorly connected or even overlapped junctions. In our patterned regrowth process, we therefore use highly reactive growth conditions. DF-TEM images of the junction areas indeed show high-quality, continuous growth of graphene between *G*¹ and *G*² areas (Fig. 1d), indicating that the crystallinity is maintained uniformly across this region without amorphous carbon or voids, within the spatial resolution of DF-TEM (around 10 nm). Furthermore, the electrical characterization across these junctions shows a low junction resistance, similar to that of the high-quality, laterally connected graphene grain boundaries reported in ref. 20.

We also find a highly reactive environment promotes uniform lateral connectivity through increased nucleation at the junction area. In Fig. 1e, we plot grain size as a function of position within the box indicated in Fig. 1c. While both *G*¹ and *G*² regions show average grain sizes of about 1.7 μm, near the junction they are much smaller (the mean is approximately 0.33 μm). The moving average (Fig. 1e, red line) shows that the width of this area with smaller grains is approximately 2 μm, comparable to the average *G*¹ and *G*² grain size. This, in addition to the increased density of small bilayer areas (bright spots in Fig. 1c and d), suggests that the junction between *G*¹ and *G*² is formed by graphene that has nucleated and grown in the junction area rather than by direct stitching between grains nucleated away from the junction area. This suggests edge-nucleated growth, which is similar to a “seeding” effect reported previously^{21–23}. In contrast, regrowth under less-reactive conditions that provide slower growth do not produce well-connected junctions in either graphene/graphene and graphene/*h*-BN films (see Supplementary Information).

¹Department of Chemistry and Chemical Biology, Cornell University, Ithaca, New York 14853, USA. ²School of Applied and Engineering Physics, Cornell University, Ithaca, New York 14853, USA. ³Kavli Institute at Cornell for Nanoscale Science, Ithaca, New York 14853, USA.

*These authors contributed equally to this work.

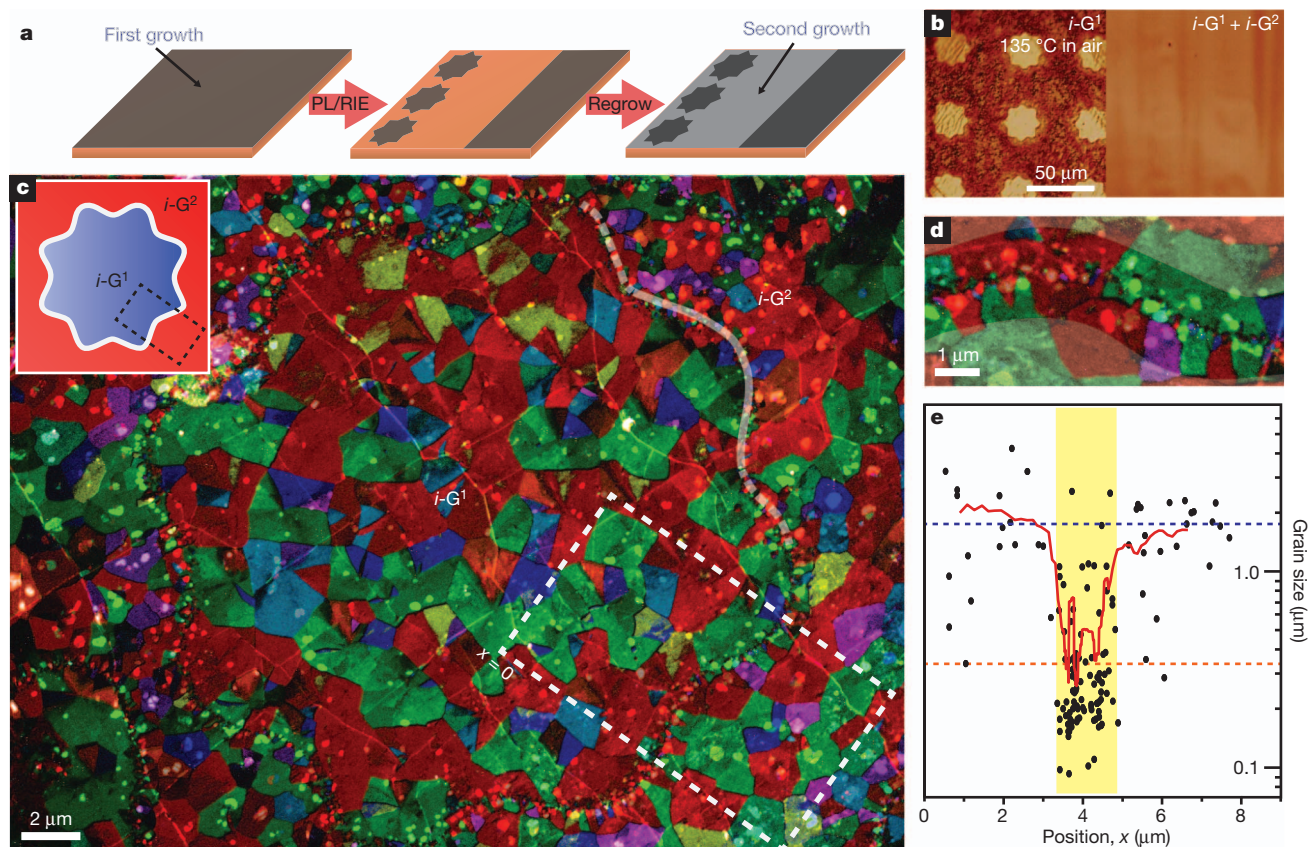


Figure 1 | Process schematic and DF-TEM characterization of graphene heterostructures. **a**, Schematic for formation of atomically thin lateral heterojunctions using photolithography (PL) and reactive ion etching (RIE). See main text for details. **b**, The left panel shows an optical image of a patterned Cu/G¹ foil oxidized to enhance contrast (the dark areas are Cu). The right panel shows an optical image after reduction of CuO_x and subsequent growth of

intrinsic-G² (*i*-G²). **c**, False-colour DF-TEM image of an *i*-G¹/*i*-G² patterned area (schematic in inset). **d**, Zoomed-in image of the junction region. **e**, Plot of grain size versus position in the box outlined in **c**. Dotted lines indicate average grain size away from (blue line) and near (highlighted region and orange line) the junction. Shading indicates the width of the region with smaller grains.

The technique described above is also applicable to the formation of insulator–metal lateral junctions using graphene and *h*-BN (Fig. 2), which we now discuss (see Methods). Figure 2a shows a false-colour DF-TEM image of a single layer *h*-BN sheet—as confirmed by Raman spectroscopy and X-ray photoelectron spectroscopy (see Supplementary Information)—with relatively large domains in excess of 1 μm. Electron diffraction also shows that the film consists of single crystals with hexagonal lattice structures (Fig. 2a, inset). This *h*-BN growth, however, yields films that are mechanically discontinuous, as indicated by the dark lines in Fig. 2a (arrows; also visible in bright-field TEM, see Supplementary Information). Instead, *h*-BN grown under more-reactive conditions (higher precursor flow rate, see Methods) results in a continuous film, while exhibiting all the known characteristics of *h*-BN sheets. This is confirmed by the X-ray photoelectron spectroscopy data in Fig. 2c (upper panels; B and N in a 1:1.08 atomic ratio) and Raman spectroscopy (lower panel; *h*-BN peak).

Careful control over the length of the *h*-BN² growth allows for the synthesis of *i*-G¹/*h*-BN² sheets with high pattern fidelity, as shown by the optical image in Fig. 2b. The darker regions indicate areas of *i*-G¹ (stronger absorption), whereas the lighter regions are comprised of *h*-BN². This, as well as the two-dimensional Raman image (inset in Fig. 2b) of the graphene 2D band intensity, confirms the successful pattern transfer to the *i*-G¹/*h*-BN² hybrid sheet. Furthermore, DF-TEM of suspended films confirms a sharp junction, as is shown in Fig. 2d, where the grains of the *i*-G¹ growth (lower, coloured half) end abruptly at the interface with the *h*-BN² (upper half). Both the bright-field TEM (Supplementary Information) and scanning electron microscopy (SEM) images (Fig. 2e) show a mechanically continuous sheet that is cleanly suspended with no breaks or tears at the junction region,

confirming the stability and integrity of these growths. We have observed similar mechanical continuity for both *i*-G¹/*i*-G² and *n*-G¹/*i*-G² growths (see Supplementary Information).

The composition of G/*h*-BN heterojunctions at the nanometre scale was investigated by cross-sectional imaging and chemical mapping of the *i*-G¹/*h*-BN² interface using an aberration-corrected scanning transmission electron microscope (STEM) and electron energy loss spectroscopy (EELS). For this, using a focused ion beam, a thin ($\sim 30 \pm 5$ nm) slice containing a junction region is carved out from a film of *i*-G¹/*h*-BN² transferred onto a Si/SiO₂ substrate (see Fig. 2f). Figure 2g (upper panel) shows the resultant EELS composition maps across a junction region, where a line heterojunction is clearly seen between two neighbouring regions with homogeneous atomic concentration. The left side indicates a high level of graphitic carbon (red; *g*-C), suggesting it belongs to graphene, whereas the other side has a high concentration of boron (green) originating from *h*-BN. Significantly, an increase in intensity of boron corresponds to a decrease in *g*-C, as shown by the line profiles of the concentration of boron and *g*-C in the junction region (Fig. 2g, lower), strongly suggesting that the G/*h*-BN junction is a lateral heterojunction with a compositional transition width of less than 10 nm (see Supplementary Information).

Successful synthesis of these hybrid films allows us to fabricate electrically isolated graphene devices in a single, atomically flat sheet, which we show in Fig. 3a. We observe conducting behaviour confined to the patterned graphene areas, with the *h*-BN² showing no conductivity within the limits of our equipment (sheet resistance $R_{\text{sheet}} > 400 \text{ T}\Omega \square^{-1}$, where \square indicates a square of the material having no thickness). We also confirm that our *h*-BN is free of small

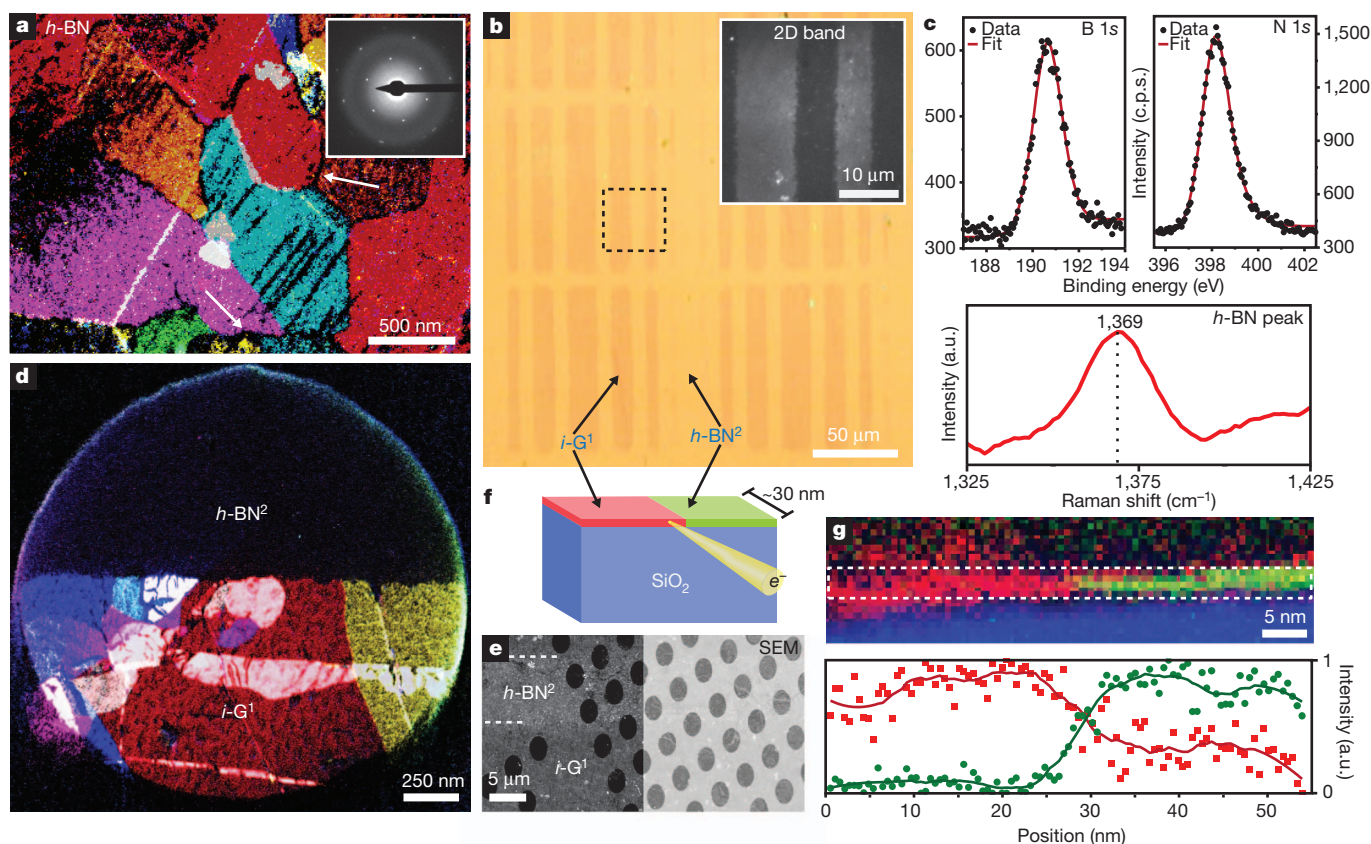


Figure 2 | *h*-BN/G heterostructure synthesis and structural characterization. **a**, False-colour DF-TEM image of an *h*-BN sheet grown in an environment of low reactivity with domains $>1\ \mu\text{m}$. Arrows indicate regions where the *h*-BN film failed to connect. Inset, representative diffraction image taken from the *h*-BN sheet, indicating hexagonal crystal structure. **b**, Optical image of an *i*-G¹ (darker areas)/*h*-BN² (lighter areas) on a Si/SiO₂ substrate. Inset, Raman graphene 2D band (area indicated by the dotted box) showing a stark contrast between the regions. **c**, X-ray photoelectron spectroscopy data (upper panels), the transition from the 1s orbital for an *i*-G¹/*h*-BN² sheet (*h*-BN² grown in a more reactive environment than **a**), showing a 1:1.08 B:N

atomic ratio. Raman spectroscopy (lower panel) confirms the presence of the *h*-BN peak. **d**, False-colour DF-TEM image of a suspended *i*-G¹/*h*-BN² sheet with the junction region clearly starting at the sharp line that ends the *i*-G¹ area. **e**, SEM image of *i*-G¹/*h*-BN² film suspended over 2- μm -sized holes. Higher contrast (left panel) highlights *i*-G¹/*h*-BN² regions, whereas lower contrast (right panel) shows the suspended film. **f**, Schematic for cross-sectional STEM EELS. **g**, The upper panel shows the elemental map of an *i*-G¹/*h*-BN² junction region containing graphitic carbon (red; g-C), boron (green), and oxygen (blue). The lower panel shows the intensity profile of g-C and boron, indicating no voids or overlap in the junction region.

conducting pockets of *h*-BNC (boron-nitride-carbon) that might form during growth¹⁰ using electrostatic force microscopy (EFM) (Supplementary Information and Fig. 3c, right). The EFM phase shift is highly uniform within both the *i*-G¹ and *h*-BN² regions; however, there is an abrupt change in the phase shift at the junction between *i*-G¹ and *h*-BN² owing to the different electrical conductivities of these materials, indicating very little carbon contamination bleeding into the *h*-BN² region.

These sheets are particularly useful for ultraflat three-dimensional electronics²⁴, where alternating *h*-BN and graphene regions can act as a wire array connected by lateral insulators. Because such an array maintains a uniform thickness throughout, the device will remain flat even after multiple transfers of such sheets without any post-processing, such as chemical mechanical polishing. We demonstrate this in Fig. 3b and c, where we fabricated a large sheet of *i*-G¹/*h*-BN² lines and performed multiple transfers onto a single substrate. After transferring the first sheet, a second was placed perpendicular to the first, with each layer contacted by electrodes. Optical images (Fig. 3b) show the structural uniformity of the final devices at different scales. The flatness and electrical properties of one such graphene-graphene crossed junction (inset in Fig. 3b), is studied by atomic force microscopy (AFM) height (Fig. 3c, left panel) and EFM phase (Fig. 3c, right panel) measurements. Topographically, region A (*h*-BN on *h*-BN) is almost indistinguishable from region B (*h*-BN on graphene), as shown by the height histograms from each region. This contrasts with the

EFM phase image, where both the bottom and top graphene strips are detected with nearly identical phase shifts. The small difference between the EFM phases of the two areas nevertheless indicates that the *h*-BN on top of the bottom graphene strip is acting as a dielectric film (see Supplementary Information). Electrical measurements (Fig. 3c, right panel) of these connections show a negligible addition of a contact resistance, confirming that such films behave as atomically flat three-dimensional interconnects. Although the vertical tunnelling current through one layer of *h*-BN is significant^{25,26}, few-layer *h*-BN formed by additional transfers could be used to electrically isolate devices vertically as well, and allow fabrication of other passive elements, such as capacitors²⁷.

Unlike G/*h*-BN structures, however, electrically conductive heterojunctions require characterization and optimization of the junction resistance. For this purpose, we fabricated arrays of devices that contained zero to four *i*-G¹/*i*-G² junctions. A false-colour SEM of an example cross-junction device is shown in Fig. 4a. The sheet resistance at the Dirac point (R_{Dirac}) for each device was measured using top-gated four-terminal measurements (Fig. 4b) and compiled for statistical comparison (Fig. 4c). Devices with (orange; 15 devices) and without (grey; 19 devices) junctions show both narrow distributions of R_{Dirac} , as well as similar medians (no junction: $6.6\ \text{k}\Omega\ \square^{-1}$; cross-junction: $6.9\ \text{k}\Omega\ \square^{-1}$). This shows that the electrical properties of heterojunction devices are similar to that of devices without junctions, despite the presence of many smaller grains in the junction area

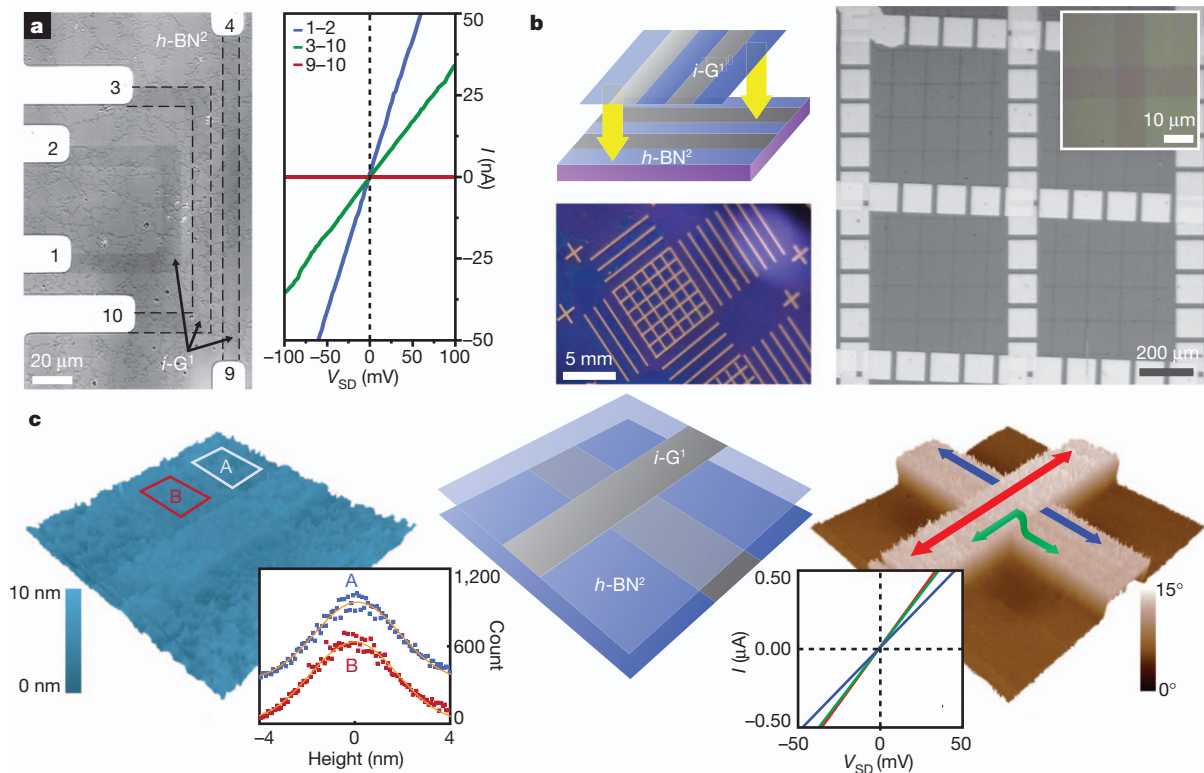


Figure 3 | *h*-BN/graphene electrical measurements. **a**, The left panel is an optical image of an *i*-G¹/*h*-BN² sheet with electrodes contacting graphene strips (outlined by dotted lines). The numbers label the electrodes (also shown in the right panel for the current–voltage (*I*–*V*) curves). The right panel shows two-terminal *I*–*V* characteristics of the indicated devices, with graphene showing conducting behaviour and *h*-BN exhibiting insulating characteristics ($R_{\text{sheet}} > 400 \text{ T}\Omega \square^{-1}$). **b**, The upper left panel is a schematic of a multiple transfer process for ultraflat three-dimensional interconnects. The lower left panel, right panel, and inset are optical images of increasing magnification of

final device substrate with each layer contacted by electrodes. **c**, The middle panel is a schematic of a G¹–G¹ cross-junction. The left panel is an AFM height image of the cross. Region A (*h*-BN on *h*-BN) is virtually indistinguishable from region B (*h*-BN on graphene), as indicated by the histogram (inset). The right panel is an EFM phase image of the same junction. Both graphene strips are visible. Two-terminal *I*–*V* characteristics (inset; $R_{\text{sheet}} < 3 \text{ k}\Omega \square^{-1}$) show no additional contact resistance owing to the graphene–graphene contact. Coloured arrows correspond to the *I*–*V* measurements in the inset.

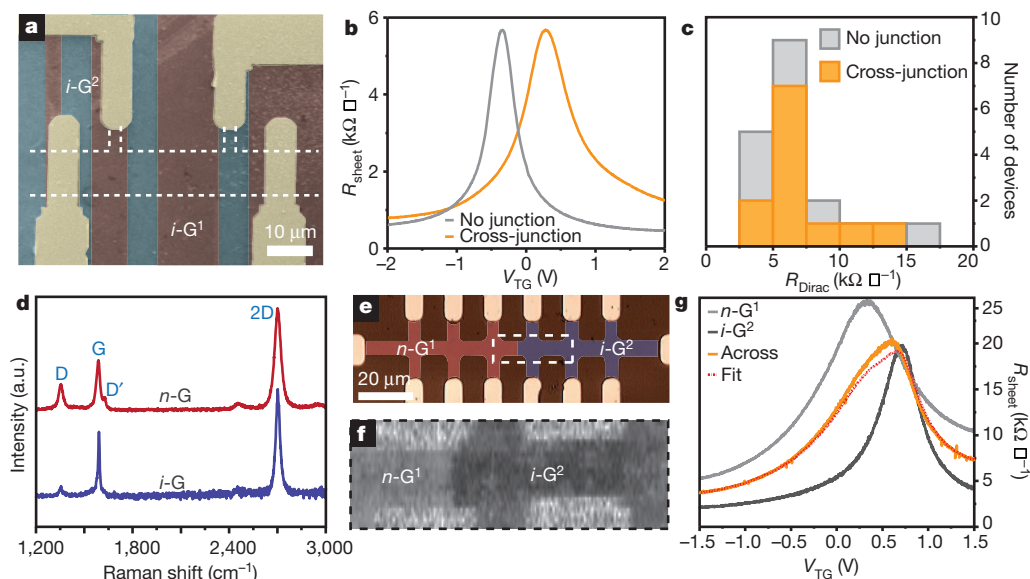


Figure 4 | Graphene junctions and heterostructures. **a**, SEM image with false-colour overlay of an *i*-G¹ (red)/*i*-G² (blue) cross-junction device before patterning. The final device area is indicated by the dashed lines. Cross-junction devices contained 1–4 junction regions. **b**, Four-terminal top gate (TG) dependence for devices without (grey) and with (orange) *i*-G¹/*i*-G² junctions, showing very similar peak resistances. **c**, Histograms of Dirac-point sheet resistance (R_{Dirac}) for devices with and without junction regions. **d**, Raman

spectroscopy of *n*-doped (*n*-G) and *i*-G growths (both synthesized in second step in order to allow direct comparison). **e**, Optical image with false-colour overlay of a heterojunction device. **f**, Two-dimensional Raman mapping of the ratio of the integrated D' and G peaks for the boxed area in **e**. **g**, Gate dependence of the junction region shows good agreement with an area-weighted average of the homogenous regions (red line, $\Delta R_{\text{junction}} \approx 0.15 \text{ k}\Omega \mu\text{m}$).

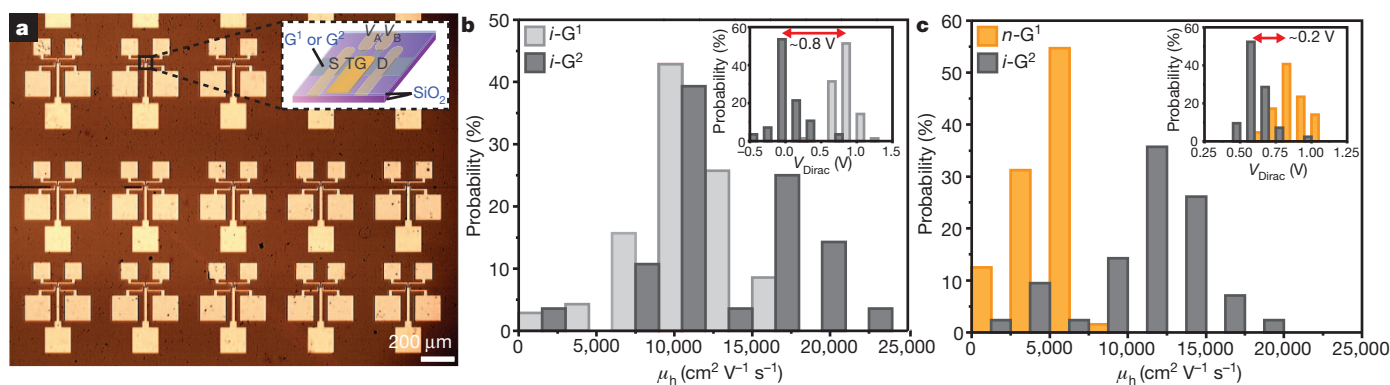


Figure 5 | Graphene device arrays and statistics. **a**, Optical image of an array of graphene transistors with device schematic (inset). **b**, Probability distribution of hole mobilities (μ_h) for $i\text{-G}^1$ (70 devices) and $i\text{-G}^2$ (28 devices) arrays. Inset, probability distribution of the Dirac point for each array showing

(Fig. 1). Additionally, field-effect carrier mobilities near the Dirac point remain high ($>10,000 \text{ cm}^2 \text{ V}^{-1} \text{ s}^{-1}$) for both types of devices, which is consistent with the properties of electrically transparent, laterally connected grain boundaries grown under reactive growth conditions²⁰.

Our method thus allows for the growth of doped heterostructures, such as p–n junctions, within a single sheet of graphene, which could enable the production of active components with mechanically and electrically continuous junctions. Figure 4e shows a false-colour optical image of a device with two differently doped graphene areas ($n\text{-G}^1/i\text{-G}^2$). The n -doped graphene area exhibits an additional D' peak (due to the presence of substitutional nitrogen dopants; Fig. 4d, red curve) that is not typically seen in $i\text{-G}$ growths (blue curve). The location of the junction region was thus confirmed using two-dimensional Raman mapping of the ratio of the integrated D' and G peaks (Fig. 4f), where the $n\text{-G}^1$ region is much brighter⁵. Electrical measurements within and across these regions again confirm electrical continuity across this region. Using top gates (5 nm Cr/45 nm Au, 100 nm of evaporated SiO_2) we measured the gate dependence in different regions, as shown in Fig. 4g ($n\text{-G}^1/i\text{-G}^2$). The device shows behaviour consistent with high-quality graphene, even across the junction region. The gate dependence of R_{sheet} in this area is in excellent agreement with an area-weighted average of the $n\text{-G}^1$ and $i\text{-G}^2$ areas with the addition of the small resistance $\Delta R_{\text{junction}} \approx 0.15 \text{ k}\Omega \mu\text{m}$ (consistent with the small junction resistance seen in Fig. 4c).

Multiple iterations of patterned regrowth would allow the formation of more complex circuits connected by lateral heterojunctions, whereas multiple transfers of these films would produce vertical heterojunctions and interconnects for increased functionality. To realize more complicated structures, it is essential that the electrical properties of sheets grown at different steps are affected by the processing in a reproducible manner. In Fig. 5, we show statistics for intrinsic (both $i\text{-G}^1$ and $i\text{-G}^2$) and n -doped graphene device arrays (optical image shown in Fig. 5a), which exhibit high-performance electrical properties. Namely, they show high field-effect mobilities (mean $>10,000 \text{ cm}^2 \text{ V}^{-1} \text{ s}^{-1}$; Fig. 5b)²⁸ and low hysteresis (see Supplementary Information). Although we observe a slight difference between the $i\text{-G}^1$ and $i\text{-G}^2$ mobility distributions (Fig. 5b), these values are consistent with variations seen from growth to growth (see $i\text{-G}^2$ in Fig. 5c), suggesting that high electrical performances could be generally achieved even after multiple regrowth processes. In addition, the Dirac point shows a narrow distribution within each area for both intrinsic and n -doped graphene growths (see insets to Fig. 5b and c). There is a shift of around 0.8 V between the Dirac-point distribution of the $i\text{-G}^1$ and $i\text{-G}^2$ growths (inset to Fig. 5b); however, the magnitude of this shift is reduced when the first growth is n -doped ($\sim 0.2 \text{ V}$, inset

a difference (0.8 V) in the mean position. **c**, Probability distribution of μ_h for $n\text{-G}^1$ (orange; 65 devices) and $i\text{-G}^2$ (grey; 43 devices) regions. Inset, the Dirac-point distributions are now much closer to the $i\text{-G}^2$ reference (0.2 V).

to Fig. 5c). Although this is consistent with the expected effects of n -doping, the overall device appears to remain p -type, probably owing to the effects of the fabrication process. Thus, improvement in the transfer and fabrication steps should lead to increased control over not only the Dirac-point distributions, but also general homogeneity^{29,30}.

We propose that our patterned regrowth technique provides a versatile and scalable method for growing and integrating layered materials, beyond $h\text{-BN}$ and graphene, for atomically thin circuitry. In particular, the addition of two-dimensional semiconducting materials, such as MoS_2 (ref. 31), would bring together the three key building blocks (insulator, metal and semiconductor) of modern integrated circuitry into a single, transferrable film. Furthermore, the devices made using this approach are likely to remain mechanically flexible and optically transparent, allowing transfer to arbitrary substrates for flexible, transparent electronics.

METHODS SUMMARY

Patterned regrowth. Synthesis of graphene and $h\text{-BN}$ were carried out in a helium-leak-checked semiconductor grade tube furnace using 25- μm -thick Cu as the growth substrate. Graphene growths were performed at $1,000^\circ\text{C}$, using the general methods reported in refs 4 and 5. For intrinsic graphene ($i\text{-G}$) flow rates were H_2 : 100 standard $\text{cm}^3 \text{ min}^{-1}$, CH_4 : 6 standard $\text{cm}^3 \text{ min}^{-1}$. For n -doped graphene ($n\text{-G}$) the flow rates were H_2 : 100 standard $\text{cm}^3 \text{ min}^{-1}$, CH_4 : 2 standard $\text{cm}^3 \text{ min}^{-1}$, NH_3 : 7 standard $\text{cm}^3 \text{ min}^{-1}$. For the first growth (G^1), Cu substrates were annealed in H_2 at $T = 1,000^\circ\text{C}$ for 1 h before introduction of CH_4 . Photolithography was then performed directly on the Cu substrate in order to pattern a protective layer of photoresist. An O_2 reactive ion etch (100 W, 105 s) was used to remove the unwanted graphene from the surface. The patterned Cu was then immediately placed in Microposit Remover 1165 to thoroughly clean the surface of residual photoresist. Immediately after this, the substrates were placed directly back into the reaction chamber for the second graphene or $h\text{-BN}$ growth. For the second growth, samples were exposed to growth reactants upon reaching the growth temperature. $h\text{-BN}$ syntheses were carried out for 5–15 min by sublimation of the ammonia-borane, as in ref. 9. For the 'slow' growth $h\text{-BN}$ (Fig. 2a), the effective flow rate from the precursor was about 1 standard $\text{cm}^3 \text{ min}^{-1}$. For the 'fast' growth, the flow rate was increased to about 4 standard $\text{cm}^3 \text{ min}^{-1}$. We did not use an additional carrier gas because this led to thicker films.

Received 16 March; accepted 10 July 2012.

- Novoselov, K. S. *et al.* Electric field effect in atomically thin carbon films. *Science* **306**, 666–669 (2004).
- Novoselov, K. S. *et al.* Two-dimensional gas of massless Dirac fermions in graphene. *Nature* **438**, 197–200 (2005).
- Zhang, Y., Tan, Y.-W., Stormer, H. L. & Kim, P. Experimental observation of the quantum Hall effect and Berry's phase in graphene. *Nature* **438**, 201–204 (2005).
- Li, X. *et al.* Large-area synthesis of high-quality and uniform graphene films on copper foils. *Science* **324**, 1312–1314 (2009).
- Zhao, L. *et al.* Visualizing individual nitrogen dopants in monolayer graphene. *Science* **333**, 999–1003 (2011).
- Jin, Z., Yao, J., Kittrell, C. & Tour, J. M. Large-scale growth and characterizations of nitrogen-doped monolayer graphene sheets. *ACS Nano* **5**, 4112–4117 (2011).

7. Kubota, Y., Watanabe, K., Tsuda, O. & Taniguchi, T. Deep ultraviolet light-emitting hexagonal boron nitride synthesized at atmospheric pressure. *Science* **317**, 932–934 (2007).
8. Kim, K. K. *et al.* Synthesis of monolayer hexagonal boron nitride on Cu foil using chemical vapor deposition. *Nano Lett.* **12**, 161–166 (2012).
9. Song, L. *et al.* Large scale growth and characterization of atomic hexagonal boron nitride layers. *Nano Lett.* **10**, 3209–3215 (2010).
10. Ci, L. *et al.* Atomic layers of hybridized boron nitride and graphene domains. *Nature Mater.* **9**, 430–435 (2010).
11. Liu, Y., Bhowmick, S. & Yakobson, B. I. BN white graphene with “colorful” edges: the energies and morphology. *Nano Lett.* **11**, 3113–3116 (2011).
12. Pruneda, J. M. Origin of half-semimetallicity induced at interfaces of C-BN heterostructures. *Phys. Rev. B* **81**, 161409 (2010).
13. Miyamoto, Y., Rubio, A., Cohen, M. & Louie, S. Chiral tubules of hexagonal BC₂N. *Phys. Rev. B* **50**, 4976–4979 (1994).
14. Wehling, T. O. *et al.* Molecular doping of graphene. *Nano Lett.* **8**, 173–177 (2008).
15. Williams, J. R., Dicarolo, L. & Marcus, C. M. Quantum Hall effect in a gate-controlled p-n junction of graphene. *Science* **317**, 638–641 (2007).
16. Dresselhaus, M. S., Jorio, A., Hofmann, M., Dresselhaus, G. & Saito, R. Perspectives on carbon nanotubes and graphene Raman spectroscopy. *Nano Lett.* **10**, 751–758 (2010).
17. Chen, S. *et al.* Oxidation resistance of graphene-coated Cu and Cu/Ni alloy. *ACS Nano* **5**, 1321–1327 (2011).
18. Huang, P. Y. *et al.* Grains and grain boundaries in single-layer graphene atomic patchwork quilts. *Nature* **469**, 389–392 (2011).
19. Kim, K. *et al.* Grain boundary mapping in polycrystalline graphene. *ACS Nano* **5**, 2142–2146 (2011).
20. Tsen, A. W. *et al.* Tailoring electrical transport across grain boundaries in polycrystalline graphene. *Science* **336**, 1143–1146 (2012).
21. Yu, Q. *et al.* Control and characterization of individual grains and grain boundaries in graphene grown by chemical vapour deposition. *Nature Mater.* **10**, 443–449 (2011).
22. Sun, Z. *et al.* Growth of graphene from solid carbon sources. *Nature* **468**, 549–552 (2010).
23. Kim, Y.-J., Lee, J.-H. & Yi, G.-C. Vertically aligned ZnO nanostructures grown on graphene layers. *Appl. Phys. Lett.* **95**, 213101 (2009).
24. Dean, C. R. *et al.* Boron nitride substrates for high-quality graphene electronics. *Nature Nanotechnol.* **5**, 722–726 (2010).
25. Britnell, L. *et al.* Electron tunneling through ultrathin boron nitride crystalline barriers. *Nano Lett.* **12**, 1707–1710 (2012).
26. Lee, G.-H. *et al.* Electron tunneling through atomically flat and ultrathin hexagonal boron nitride. *Appl. Phys. Lett.* **99**, 243114 (2011).
27. Sanchez-Yamagishi, J. *et al.* Quantum Hall effect, screening, and layer-polarized insulating states in twisted bilayer graphene. *Phys. Rev. Lett.* **108**, 076601 (2012).
28. Meric, I. *et al.* Current saturation in zero-bandgap, top-gated graphene field-effect transistors. *Nature Nanotechnol.* **3**, 654–659 (2008).
29. Moser, J., Barreiro, A. & Bachtold, A. Current-induced cleaning of graphene. *Appl. Phys. Lett.* **91**, 163513 (2007).
30. Liang, X. *et al.* Toward clean and crackless transfer of graphene. *ACS Nano* **5**, 9144–9153 (2011).
31. Radisavljevic, B., Radenovic, A., Brivio, J., Giacometti, V. & Kis, A. Single-layer MoS₂ transistors. *Nature Nanotechnol.* **6**, 147–150 (2011).

Supplementary Information is available in the online version of the paper.

Acknowledgements We thank P. McEuen and M. Spencer for discussions. This work was mainly supported by AFOSR grants (FA9550-09-1-0691 and FA9550-10-1-0410) and the NSF through the Cornell Centers for Materials Research (NSF DMR-1120296), which also provided the electron microscopy facilities. Additional funding was provided by the Alfred P. Sloan Foundation. L.B. was partially supported by a Fullbright scholarship; R.W.H. and P.Y.H. were supported by an NSF Graduate Research Fellowship. Device fabrication was performed at the Cornell NanoScale Facility, a member of the National Nanotechnology Infrastructure Network, which is supported by the National Science Foundation (grant ECS-0335765).

Author Contributions M.P.L. and C.-J.K. contributed equally to this work. Synthesis, device fabrication, and electrical measurements and analysis were done by M.P.L. and C.-J.K. DF-TEM and data analysis were performed by L.B. and C.-J.K. EELS measurement and data analysis were conducted by P.Y.H. and D.A.M. Raman measurements and analysis were carried out by M.P.L. with assistance from R.W.H. J.P. designed the experiments and oversaw the research. M.P.L. and J.P. wrote the manuscript with assistance from R.W.H. and input from all authors.

Author Information Reprints and permissions information is available at www.nature.com/reprints. The authors declare competing financial interests: details are available in the online version of the paper. Readers are welcome to comment on the online version of the paper. Correspondence and requests for materials should be addressed to J.P. (jpark@cornell.edu).